Numerical flow visualization of a single large-sized bubble in turbulent Couette flow using *OpenFOAM*

Sangwon Kim [a], Nobuyuki Oshima [b], Hyun Jin Park [c]

[a] *RIKEN Center for Computational Science, RIKEN, Kobe, Japan*

[b] *Computational Fluid Mechanics Laboratory, Faculty of Engineering, Hokkaido University, Sapporo, Japan*

[c] *Laboratory for Flow Control, Faculty of Engineering, Hokkaido University, Sapporo, Japan*

Corresponding Author:

Sangwon Kim, Ph.D.

RIKEN Center for Computational Science, RIKEN

7 Chome-1-26, Minatojima, Minamimachi, Chuo Ward, Kobe, Hyogo, 650-0047, Japan

Tel: +81-70-1546-7449

Fax: +81-11-706-6724

E-mail: sangwon.kim@riken.jp

Abstract

Owing to different flow conditions—for example, Poiseuille and Couette flow—one could expect different deformations of large-sized bubbles; however, bubble dynamics has been mostly investigated in channel flow. Consequently, an intermediate flow condition shared by both the channel and ship surface is needed for large-sized bubbles, although it can be difficult to simultaneously generate turbulent Couette flow in the channel and measure the shear stress on the ship's surface experimentally. In this study, large-sized bubbles in turbulent Couette flow were investigated numerically to determine their common characteristics under such flow conditions. The *interIsoFoam* solver from *OpenFOAM*—which can directly capture the interface via the geometric volume of fluid method—was used to conduct the simulations of the gas–liquid interface problem. The turbulent Couette flow was driven by top wall velocity condition with an initial perturbation, and three different bubble sizes with Weber numbers in the range of 200–300 were chosen to determine the characteristics of large-sized bubbles. By monitoring the results according to bubble size, we could determine bubble characteristics that were distinguishable from those in turbulent Poiseuille flow. Consequently, bubble deformation was dominated by the velocity gradient and shear rate, which was greater than that during single-phase flow from the liquid-film region. These results allowed us to generalize the deformation mechanism of large-sized bubbles in turbulent Couette flow into five categories—namely, the initial shape, deformation on the front side, change of the center of gravity, pinch-off/breaking of the ligament, and deformation to a stable shape.

Keywords: Two-phase flow, large-sized bubble, turbulent Couette flow, direct numerical simulation, *OpenFOAM*

1. Introduction

Large-sized bubbles—that is, those larger than 1 mm in diameter—have attracted industrial attention as components for air lubrication systems designed to reduce the drag of ships, as they are easier and less expensive to generate than microbubbles (McCormick and Bhattacharyya, 1973; Madavan *et al*., 1985; Merkle and Deustch, 1992; Kodama *et al*., 2000) and air film methods (Fukuda *et al*., 1999; Katsui *et al*., 2003; Mäkiharju *et al*., 2013). The idea of using large-sized bubbles arose because the air injected along a ship's bottom surface tends to form millimeter-sized bubbles owing to the balance between the strong shear of the boundary layer and the surface tension of the bubbles (Hinze, 1955; Sanders *et al*., 2006; Johansen *et al*., 2010). Murai *et al*. (2006) reported that large-sized bubbles provided a velocity gradient that calmed the wake region. The performance of large-sized bubbles for bubble drag reduction (BDR) was later found to depend on the bubble length (Murai *et al*., 2007; Oishi and Murai, 2014). In addition to the velocity gradient in the wake region, the liquid film between the bubbles and wall was found to reduce skin friction by relaminarizing the flow in the film. From this viewpoint, Park *et al*. (2019) experimentally investigated the relationship between film thickness and BDR. The physical mechanism of the large-sized bubble drag reduction effect originates from its deformation, which can be induced by complex parameters such as the shear stress around the bubble and its buoyancy. Murai (2014) reported additional details regarding flow physics.

These BDR studies in horizontal flow were conducted in a horizontal channel to investigate the bubble flow characteristics or control parameters of BDR (Park *et al*., 2009, 2015, 2022; Tanaka *et al*., 2021), as well as in model ship tests to find an effective BDR condition for practical applications (Park *et al*., 2016, 2018; Tanaka *et al*., 2020). In applying our understanding vis-à-vis air bubbles in horizontal channel flow to ship air lubrication systems, it would be necessary to consider the difference in flow conditions between the horizontal channel and ships because the driving principles of these flows are different—for example, horizontal channel flow, or Poiseuille flow, is induced by pressure gradients, as shown in **Fig. 1(a)**, whereas a ship's surface flow, or Couette flow, is induced by the wall velocity, as shown in **Fig. 1(b)**.

These two different flow conditions are also controversial in single-phase flow and have been previously studied in horizontal turbulent channel flow (Orlandi *et al*., 2015; Andreolli *et al*., 2021). Bubble characteristics in these flows can differ, especially those of deformable bubbles. A comparison between bubble characteristics under these two different flow conditions in the same flow domain—such as the horizontal channel condition—could be used to explain any unclear aspect. Meanwhile, several problems in generating turbulent Couette flow have been observed in experiments on horizontal channel flow. Turbulent Couette flow generation requires a long channel and a complicated instrument for moving walls—such as a conveyor belt—which can hinder the measurement of the skin friction of the top wall. Consequently, most of the Couette flow for two-phase flow is laminar and driven by the motion of the top and bottom walls (Müller-Fischer *et al*., 2008), this phenomena have been investigated using other methods—such as the Taylor–Couette flow method—on microbubbles, which have relatively small buoyancy forces (Fokoua *et al*., 2015; Murai *et al*., 2008, 2018).

However, a large-sized bubble has a high buoyancy force, which is important in determining its shape. For instance, the direction of the buoyancy force is in the spanwise direction of the flow in the Taylor–Couette flow model, while it is in the wall-normal direction in channel flow. Consequently, it can be difficult to identify the same characteristics observable in channel flow under Taylor–Couette flow conditions. These problems in generating turbulent Couette flow in a horizontal channel can be solved via numerical simulation because Couette flow is mathematically simpler than Poiseuille flow. In the present study, a direct numerical simulation of turbulent Couette flow with a single large-sized bubble of varying size was performed to examine the bubble characteristics—such as deformation and flow—inside the liquid film.

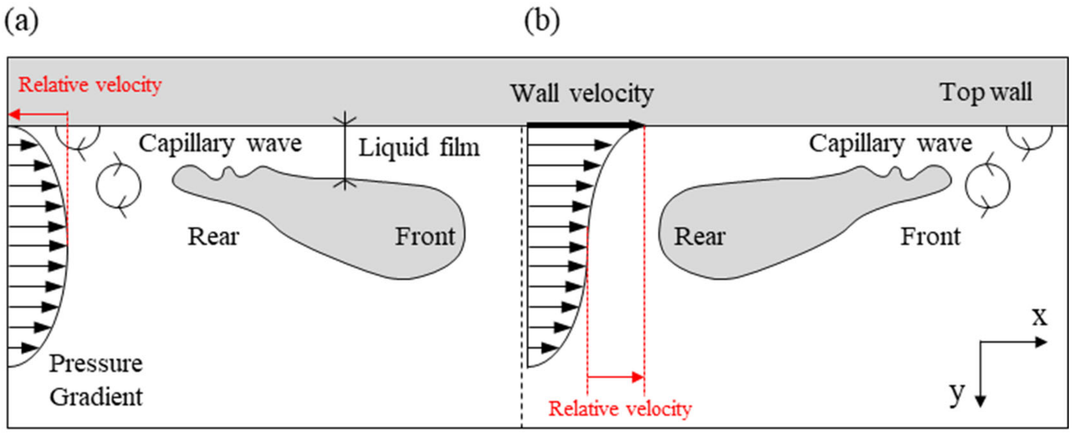

Fig. 1 Schematic of large-sized bubble formation under different flow conditions, (a) turbulent Poiseuille flow, (b) turbulent Couette flow.

2. Characteristics of a large-sized bubble and domain description

A schematic of large-sized bubble formation under Poiseuille and Couette flow conditions is shown in **Fig. 1**. Generally, the surrounding of a single large-sized bubble under horizontal turbulent flow can be divided into the liquid film between the wall and bubble, the capillary wave on the bubble surface at the rear of the liquid film, the secondary flow from the bubble wake, and the bubble shape between the front and rear sides. Herein, bubble characteristics under Couette flow can be expected to form in opposite directions than under Poiseuille flow owing to the direction of the relative velocity from the center of the channel with respect to the wall velocity.

The experimental channel setup of Oishi and Murai (2014) is shown in **Fig. 2(a)**. The test section is 6000 mm in length, and a fully developed boundary layer is generated before the bubble is injected into the channel. The channel width is 100 mm to prevent the effect of the interaction between the boundary layer and the sidewall. In this study, the flow geometry and coordinate system of the numerical simulation is as shown in **Fig. 2(b)**; the length and width of the computational domain can be shortened using periodic conditions in the streamwise and spanwise directions to reduce computational resource consumption and eliminate the sidewall effects. Based on the experimental conditions, the dimensions of the domain are as follows: height ($H = 2h$) = 10 mm, where h is the half-height of the channel, length (L) = 100 mm, and width (W) = 70 mm. For the mesh condition, the total number of grid points is 29,970,336 (404 × 66 × 562 in the x-, y-, and z-directions, respectively). In detail, the grid spacings in the streamwise and spanwise directions are $\Delta x^+ = 12.87$ and $\Delta z^+ = 6.47$, respectively, and non-uniform grids are applied in the wall-normal direction. The first grid point away from the wall is at $\Delta y^+ = 0.54$, and the maximum grid size is $\Delta y^+ = 12.84$ from the centerline of the channel.

Table 1 lists the experimental and numerical conditions used in the present study along with those used in previous studies (Oishi and Murai, 2014; Kim *et al.*, 2021), including the channel size. To generate turbulent Couette flow in the channel, the velocity of the top wall in the channel (U_{wall}) is applied to obtain the same friction velocity (u_τ) used in the previous studies; this facilitates a comparison of the bubble characteristics and drag reduction performance in future investigations. All dimensionless numbers are obtained based on single-phase flow conditions.

Table 1 Comparison of the experimental and numerical conditions used in this study and in the literature.

	Oishi and Murai (2014)	**Kim *et al.* (2021)**	**Present study**
Flow condition	Poiseuille flow	Poiseuille flow	Couette flow
$L \times H \times W$ [mm]	6000 × 10 × 100	100 × 10 × 70	100 × 10 × 70
ρ [kg/m^3]	998.7	998.7	998.7
ν [m^2/s]	1.08×10^{-6}	1.08×10^{-6}	1.08×10^{-6}
U_{mean} [m/s]	1.0	1.039	1.11
U_{wall} [m/s]	–	–	2.16
Fr	3.19	3.31	3.54
Re	9260	9620	10278
Re_τ	260	260	260

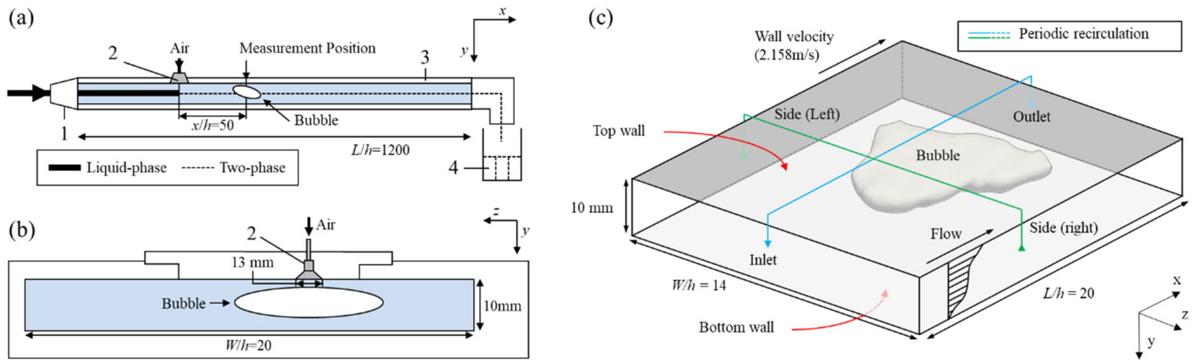

Fig. 2 Schematic of the experimental and numerical conditions used in (a) Oishi and Murai (2014) and (b) the present study.

3. Numerical Methods

3.1 Volume of fluid method

The volume of fluid (VOF) method is a Eulerian volume tracking method in which a step α function is used to mark the volume fraction of the tracked phase in a control volume. The first advantage of the VOF method for the numerical simulation of large-sized bubbles is the conservation of mass by construction, which is crucial for addressing long-term calculations over a relatively large interfacial area. The second advantage is that the Eulerian framework of the VOF method allows the handling of large deformations and topological changes without requiring additional algorithms. This simplifies the results of bubble coalescence or breakup through a different field indicator distribution, especially when simulating large-sized bubbles that frequently show large deformations at the interface. The VOF method uses the continuity and momentum equations as the governing equations, as shown in **Eqs. (1)** and **(2)**, respectively, as well as the transport equation of the volume fraction α, expressed as shown in **Eq. (3)**. The advection equation of α enables the use of only one equation in the entire flow domain to describe the local properties, instead of applying a different set of equations to each phase. The volume fraction α can be averaged in each of the mesh cells, the interface between phases is found in cells where $0 < \alpha < 1$. Fluid properties, such as the density in the cells, can be calculated using α as a weighted average, as shown in **Eq. (4)**.

$$\nabla \cdot \boldsymbol{u} = 0 \tag{1}$$

$$\frac{\partial \rho \boldsymbol{u}}{\partial t} + \rho \nabla \cdot (\boldsymbol{u}\boldsymbol{u}) = -\nabla p + \nabla \cdot \mathbf{T} + \rho \mathbf{f} + \rho \mathbf{f}_g \tag{2}$$

$$\frac{\partial \alpha}{\partial t} + \nabla \cdot (\alpha \boldsymbol{u}) = 0 \tag{3}$$

$$\rho = \alpha \rho_{\text{water}} + (1-\alpha)\rho_{\text{air}} \tag{4}$$

The VOF method requires an additional surface capturing method to suppress the smearing of the volume fraction α from the interface cells. The *isoAdvector* method is a VOF-based geometric surface reconstruction technique that captures extremely sharp interfaces using the concept of isosurfaces. The volume fraction α in each cell C_i at time t can be expressed by the function $H(\mathbf{x}, t)$, as shown in **Eq. (5)**. Here, $H(\mathbf{x}, t)$ is an indicator field, as shown in **Eq. (6)** for time t and location $\mathbf{x}$. Additionally, the updated volume fraction α in each cell C_i from time t to $t + \Delta t$ can be formulated as described in **Eq. (7)**.

$$\alpha_{i}(t) = \frac{1}{V_{i}} \int_{C_{i}} H(\mathbf{x},t)\mathrm{d}V \tag{5}$$

$$H(\mathbf{x},t) \equiv \frac{\rho(\mathbf{x},t) - \rho_{\text{air}}}{\rho_{\text{water}} - \rho_{\text{air}}} \tag{6}$$

$$\alpha_{i}(t+\Delta t) = \alpha_{i}(t) - \frac{1}{V_{i}} \sum_{j \in B_{i}} s_{ij} \int_{t}^{t+\Delta t} \int_{F_{j}} H(\mathbf{x},\tau)\mathbf{u}(\mathbf{x},\tau) \cdot \mathrm{d}\mathbf{S}\,\mathrm{d}\tau \tag{7}$$

where B_i is the list of all faces F_j belonging to C_i, and the auxiliary factor s_{ij} is either +1 or −1 to ensure that the product $s_{ij}\mathrm{d}\mathbf{S}$ is oriented outward from F_j.

The time integral of the second term on the right-hand side of **Eq. (8)** can be replaced by the total volume fraction transported across face j from time t to $t + \Delta t$, $\Delta V_j(t,\Delta t)$, as shown in **Eq. (9)**. The *isoAdvector* method requires the estimation of $\Delta V_j(t,\Delta t)$ using α_i and $\mathbf{u}_i$, as well as the constant volumetric face flux ϕ_j in **Eq. (9)**. A more detailed description of the *isoAdvector* method is available in Roenby *et al*. (2016) and Gamet *et al*. (2020).

$$\Delta V_{j}(t,\Delta t) \equiv \int_{t}^{t+\Delta t} \int_{F_{j}} H(\mathbf{x},\tau)\mathbf{u}(\mathbf{x},\tau) \cdot \mathrm{d}\mathbf{S}\,\mathrm{d}\tau \tag{8}$$

$$\phi_{j}(t) = \int_{F_{j}} \mathbf{u}(\mathbf{x},t) \cdot \mathrm{d}\mathbf{S} \tag{9}$$

Based on the above method, large-sized bubbles in turbulent Poiseuille channel flow can be modeled numerically, with good agreement between the numerical and experimental results (Oishi and Murai, 2014; Kim *et al*., 2021).

3.2 Numerical solvers and boundary conditions

A numerical simulation was performed using the open-source computational fluid dynamics (CFD) package *OpenFOAM* v.1906. In this study, the *pimpleFoam* solver was used to generate a fully developed turbulent flow in the channel, while the *interIsoFoam* solver, which is used in the *isoAdvector* method as the interface-sharpening method, was used for two-phase flow. In short, this approach creates two divided cells within one cell containing the interface location; these cells occupy one or zero volume fractions, as controlled by the mean velocity of the cell. Further details, such as the verification of *interIsoFoam*, can be found in Kim *et al*. (2020, 2021).

All schemes used in this study provide second-order accuracy. The global time step was set to 2.0×10^{-6} s to ensure that the Courant–Friedrichs–Lewy (CFL) number remained below 0.5—the interface CFL number was less than 0.1 in each simulation. It was maintained at approximately 0.4 in a previous study as the interface CFL number frequently increased sharply owing to the large and instantaneous deformation of bubbles during bubble breakup and coalescence. Both solvers use the *Pimple* algorithm for pressure-velocity coupling in a segregated manner, whereby a velocity field is computed to satisfy the continuity and momentum equations using an iterative procedure. **Table 2** lists the boundary conditions for the computational domain. At the inlet and outlet, periodic conditions are applied to the coupling conditions between them. These boundary conditions were also applied to the side boundaries. For the wall boundaries, the *NoSlip* condition is utilized to set the velocity to zero and generate a boundary layer. The *ConstantAlphaContactAngle* condition is additionally applied for two-phase flow to prevent bubble dispersion on the top wall. The numerical procedure can be divided into three stages to accommodate the required changes in the solvers and boundary conditions—that is, stage 1, which conducts fully developed turbulent Couette flow, stage 2, which conducts bubble injection and stabilization, and stage 3, which conducts turbulent channel flow with a single injected large-sized bubble. Further details regarding this numerical procedure are reported in Kim *et al*. (2020).

Table 2 Boundary conditions and solvers used in each stage of the numerical procedure.

<table>
<tr><th>Term</th><th>Stage 1</th><th>Stage 2</th><th>Stage 3</th></tr>
<tr><td>Solver</td><td>pimpleFoam</td><td colspan="2">interIsoFoam</td></tr>
<tr><td>Top</td><td>Wall velocity (2.16 m/s)</td><td colspan="2">Wall velocity (2.16 m/s),
ConstantAlphaContactAngle (71°)</td></tr>
<tr><td>Bottom</td><td>NoSlip</td><td colspan="2">NoSlip, ConstantAlphaContactAngle (71°)</td></tr>
<tr><td>Inlet/Outlet</td><td colspan="3">Cyclic (Inlet ↔ Outlet)</td></tr>
<tr><td>Side</td><td colspan="3">Cyclic (Left ↔ Right)</td></tr>
</table>

4. Modeling of turbulent Couette flow

Figure 3 shows a schematic of the turbulent Couette flow generation in stage 1. The flow is driven by a pressure gradient to reach a bulk velocity of 1.039 m/s, as shown in **Fig. 3(a)**, because it is easier to generate the initial perturbation than only using wall velocity for the fully developed flow. Under this condition, a gap exists between the pressure gradient region and the wall to generate the initial perturbation. After achieving the target mean velocity and proper initial perturbation, the pressure gradient—which drives the channel flow—is removed, and the velocity condition (2.16 m/s) of the top wall drives the flow, as shown in **Fig. 3(b)**. Finally, a turbulent Couette flow is generated.

Figure 4 shows the numerical results of the turbulent Couette flow. It was explored by examining the profile of the dimensionless mean velocity in the streamwise direction $u^+ = (U_{\mathrm{wall}} - u)/u_\tau$ and the root-mean-square (RMS) velocity fluctuations in the streamwise and wall-normal directions, as shown in **Eq. (10)**, represented as a function of the wall distance $y^+ = yu_\tau/\nu$, where y is the distance from the top wall. In addition, the dimensionless Reynolds shear stress, represented as a function of the wall distance y/h, was examined.

$$u_{rms}^{+} = \sqrt{\overline{u'^2}}\,/u_\tau\,;\ v_{rms}^{+} = \sqrt{\overline{v'^2}}\,/u_\tau \tag{10}$$

Results from two previous studies were compared with the results of the present study. The first set of results was obtained from Oishi and Murai (2014), who used the same domain conditions as the present study, to confirm the mean velocity profile and the difference in turbulent properties. The second set was obtained from Avsarkisov *et al.* (2014), who investigated turbulent planar Couette flow in single-phase flow to determine whether the turbulent properties were well simulated for Couette flow conditions. The mean velocity and RMS velocity fluctuation in the wall-normal direction in the present study showed similar trends to those reported in both studies. From the center of the channel ($y^+ \approx 300$), the mean velocity exhibited different trends from those of Oishi and Murai (2014) because of the different flow conditions. The RMS velocity fluctuation in the streamwise direction showed trends similar to those of both the previous studies below $y^+ = 50$. However, the present RMS velocity fluctuation results were similar to but located above the results of Oishi and Murai (2014) from $y^+ = 50$, but beneath those of Avsarkisov *et al.* (2014). This velocity fluctuation deviation in the streamwise and wall-normal directions under turbulent Couette flow conditions could be expected to affect the Reynolds shear stress, which exhibited different trends in the two previous studies. The present results approach those for turbulent Couette flow, but some deviation remains, indicating that the momentum from the pressure gradient remained and hindered the momentum transfer from the near-top wall to the bulk flow and bottom of the channel. Moreover, the current mesh condition was based on the flow conditions of Kim *et al*. (2021)—that is, the channel size could be insufficient to develop a coherent turbulent structure in turbulent Couette flow, as reported by Kawata and Tsukahara (2021). Meanwhile, deformation of the upper part of a large-sized bubble and the skin friction trends depended on the velocity gradient and shear rate near the viscous sublayer and buffer layer below $y^+ = 50$ ($y/h \approx 0.2$), and present results accurately reproduced these regions. In addition, the size of a large-sized bubble is relatively larger than that of the turbulence length scale. Therefore, the local deformation at log-law region could be neglected, but we assume the entire trends are almost the same. In future work, the mesh condition should be investigated to improve the accuracy of the turbulent properties of turbulent Couette flow.

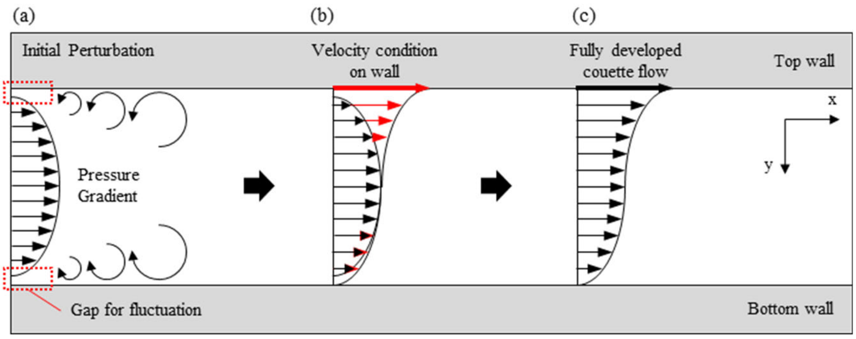

Fig. 3 Sequence of turbulent Couette flow generation (a) Initial perturbation by the pressure gradient, (b) Change from pressure gradient to velocity condition on the wall, (c) Fully developed Couette flow.

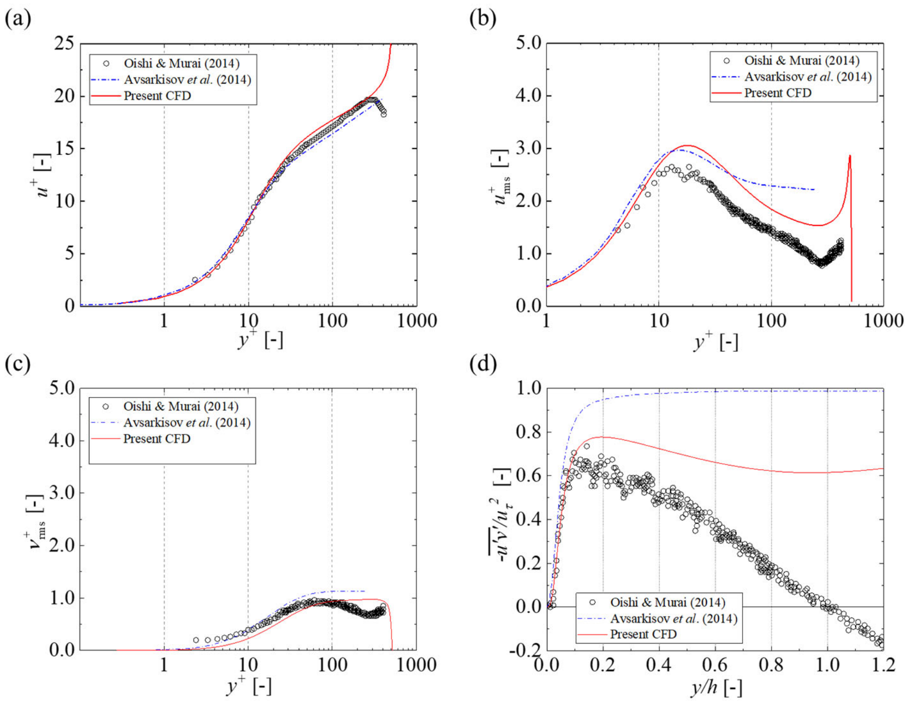

Fig. 4 Comparison of the turbulent properties between previous studies and this study. (a) Mean velocity, (b) RMS velocity fluctuation in the streamwise direction, (c) RMS velocity fluctuation in the wall-normal direction, and (d) Reynolds shear stress.

5. Numerical Results and Discussion

5.1 Characteristics of the initial bubble

In stage 2, the bubbles are injected using the *SetFields* function of *OpenFOAM*, which sets the scalar values of the fields in specific regions. To stabilize the bubble in the channel, an adjustable time step is used to maintain an interface CFL number below 0.4. When placing the bubble in the channel, as shown in **Fig. 5(a)**, a small gap is provided between the wall and the bubble interface (to represent a detached bubble); this saves computational resources by avoiding the simulation of the bubble detachment from the wall. The bubble is placed at the bottom of the channel because, when placed near the top wall, it is fragmented into small bubbles by the high shear, as shown in the top panel of **Fig. 5(b)**. Consequently, the bubble shape can be successfully maintained, as shown in **Fig. 5(c)**.

Thus, further numerical simulations were performed on the three bubble cases, as shown in **Table 3** and **Fig. 6**, and the bubble properties were obtained before the initial breakup. There are two definitions of bubble velocity—that is, the traveling velocity of the bubble $U_{tra.}$ and the relative velocity $U_{rel.}$ for the top-wall velocity, where $U_{rel.} = U_{wall} - U_{tra.}$. Thus, the Weber numbers, $We_{tra.}$ and $We_{rel.}$, were obtained using these two velocities.

The cases in the present study were for $We_{tra.}$ within 200–300, where the skin-friction drag reduction in the secondary flow and the middle of the liquid film were observed as in Kim *et al*. (2021). The bubbles over $We_{tra.} \approx 300$ were not included because they showed breakup patterns different from those of the present study, making it difficult to categorize the deformation characteristics. Consequently, the cases of the present study were established based on $We_{tra.}$ in the range of 200–300, each case having a different bubble volume. As expected from **Fig. 1**, the capillary wave region—which extends from the top of the liquid film to the edge of the bubble (colored red in **Fig. 6**)—is formed at the front of the bubble, while the rear shape of the individual bubble is round and arched. The present cases exhibit frequent oscillation and wider capillary wave region areas than those in the reference cases of Kim *et al*. (2021).

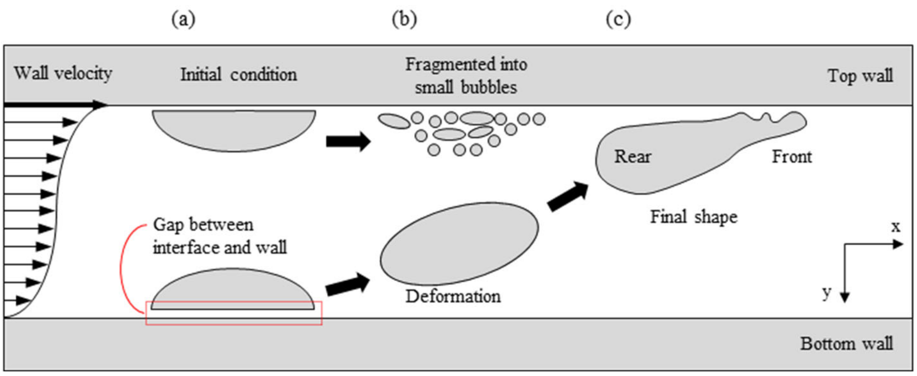

Fig. 5 Schematic of bubble injection in the channel. (a) Initial condition of a bubble when placed near the top and bottom, (b) Intermediate condition of bubble deformation according to the initial placement, and (c) Final shape of a bubble when placed at the bottom of the channel

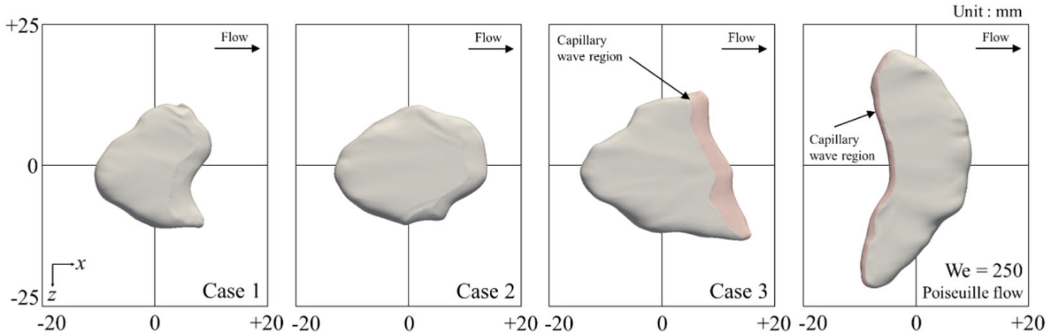

Fig. 6 Top view of the initial bubble shape for each case.

Table 3 Bubble parameters. The equivalent bubble diameter d_e is calculated from the bubble volume V_b.

		Case 1	**Case 2**	**Case 3**	**Poiseuille flow (Kim *et al*. 2021)**
Bubble volume (V_{bubble}) [mm^3]		1463.3	1912.2	2167.5	2070.5
Equivalent diameter ($D_{equiv.}$) [mm]		14.09	15.40	16.06	15.82
Bubble velocity	$U_{tra.}$ [m/s]	1.075	1.083	1.112	1.054
	$U_{tra.}$ / U_{mean}	0.968	0.976	1.002	1.015
	$U_{rel.}$ [m/s]	1.085	1.077	1.048	-
	$U_{rel.}$ /U_{mean}	0.977	0.970	0.944	-
Weber number	$We_{tra.} = \rho U_{tra.}^2 D_{equiv.}/\sigma$	232	258	283	250
	$We_{rel.} = \rho U_{rel.}^2 D_{equiv.}/\sigma$	237	255	252	-

5.2 Shape evolution and deformation characteristics of a large-sized bubble

Figures 7–9 show the top views of the time-domain bubble evolution for the different cases. The bubble shape could not be visualized in a uniform time interval as the bubble crosses the cyclic boundary conditions in the streamwise and spanwise directions and is thus divided into several parts. Consequently, the images were obtained when the bubble was located near the center or not hanging over these boundaries. Although it was difficult to determine the bubble dynamics with respect to bubble size, bubble deformation could be categorized as follows:

a) The initial state of the bubble prior to deformation, corresponding to Case 1 (0–167, 351, 410, 621, 671 ms), Case 2 (0, 59, 270, 369, 432 ms), and Case 3 (0, 500, 693 ms). The front side of the bubble is irregular, with a high curvature on the tip in the spanwise direction.

b) After the initial state, ligaments develop from the span edge of the front side of the bubble. Generally, the ligament head grows from the front and outer sides in the spanwise direction. These ligaments develop from both sides for Case 1 (261, 288 ms), Case 2 (180, 270 ms), and Case 3 (63, 122, 522–

612 ms), when the front side of the bubble is aligned perpendicular to the streamwise direction. These ligaments exhibit an imbalance between them, and smaller ligaments are frequently suppressed. By contrast, a one-direction development of the ligament can be observed in Case 1 (410–536 ms) and Case 2 (95–203, 396, 486–572 ms) when the front side of the bubble is tilted in the streamwise direction.

c) The ligament tips exhibit pinch-off and breakup, as in Case 1 (297–320, 540, 554 ms), Case 2 (243 ms), and Case 3 (243, 252, 612–666 ms). Daughter bubbles are generated and detach from the main bubbles. These daughter bubbles are typically small, considering that the major bubbles do not affect the total volume, as shown in **Table 4**, where the volume ratios of the daughter bubbles are distributed near zero. After breakup, the ligament bases experience splash-back, and the center of the air mass shifts to the center of the bubble again.

d) Not all of the ligaments experience splash-back after breakup. A ligament that is larger than one opposite of it suppresses its development. Eventually, the center of the air mass shifts to the ligament side such that the main bubble part shrinks, and the ligament expands for Case 2 (243–338 ms) and Case 3 (252–383 ms). This situation occurs without splitting, as in Case 2 (486–572 ms).

e) After the breakup from the tip of the ligaments or the shifting of the center of the air mass to the ligament side, the bubble shape deforms for shape stabilization, as in Case 1 (351, 410, 621, 671 ms), Case 2 (270, 369, 432 ms), and Case 3 (500, 693 ms). The bubble rotates from the streamwise direction owing to the direction of the development of a relatively large ligament. From this state, one direction of ligament development is frequently observed.

Table 4 Volume ratio of daughter bubbles, V_{daughter}, and major bubble, V_{major}. V_{total} is the total volume of the bubble before each breakup.

	Time [ms]	$V_{\mathrm{daughter}} / V_{\mathrm{total}}$ **[-]**	$V_{\mathrm{major}} / V_{\mathrm{total}}$ **[-]**
Case 1	297	0.04×10^{-2}	99.96×10^{-2}
	320	0.09×10^{-2}	99.91×10^{-2}
	554	0.05×10^{-2}	99.95×10^{-2}
Case 2	243	0.09×10^{-2}	99.91×10^{-2}
Case 3	252	0.91×10^{-2}	99.09×10^{-2}
	468	0.02×10^{-2}	99.98×10^{-2}
	648	4.11×10^{-2}	95.89×10^{-2}
	666	5.39×10^{-2}	94.61×10^{-2}

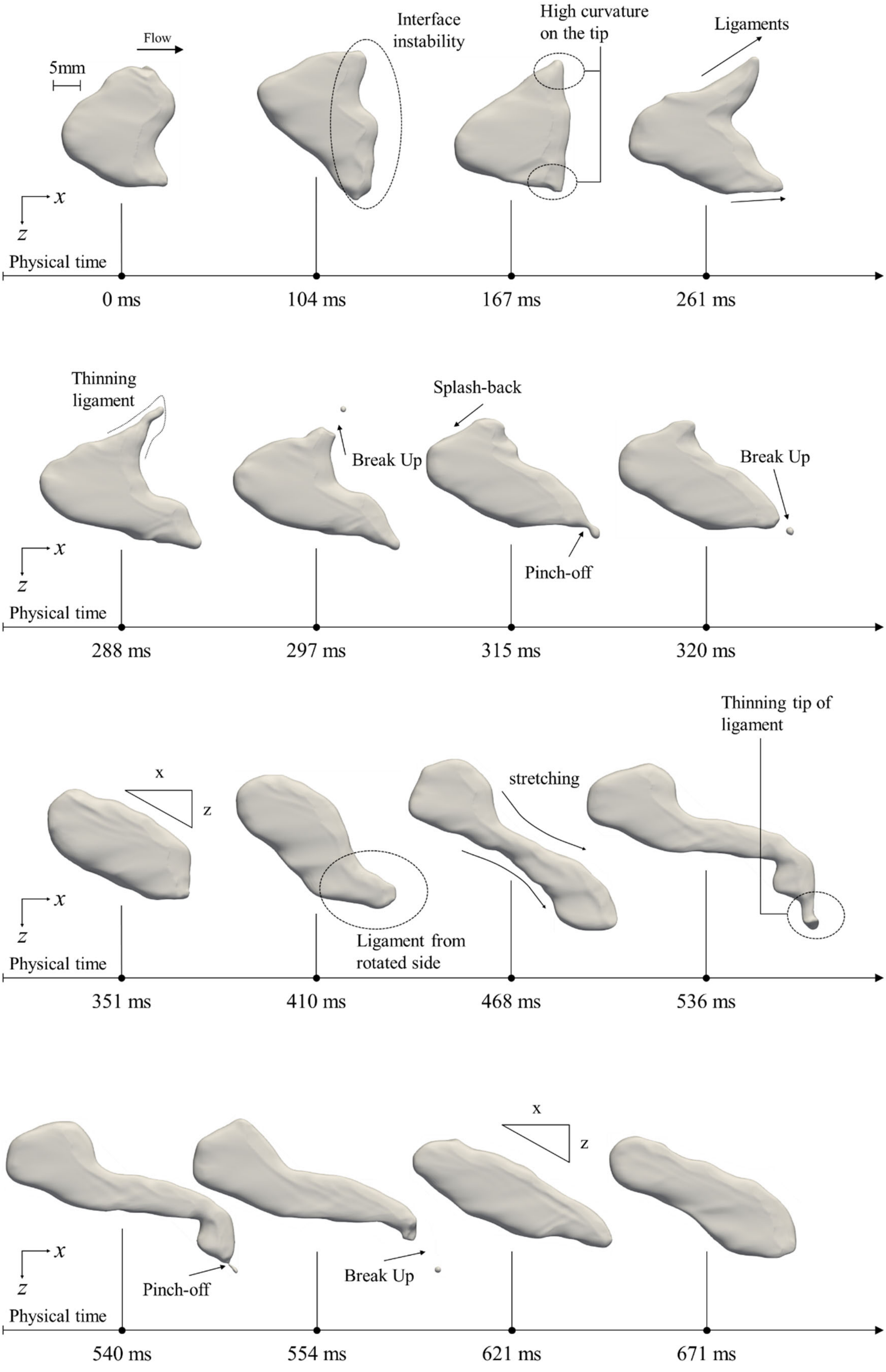

Fig. 7 Top view of the bubble shape evolution for case 1

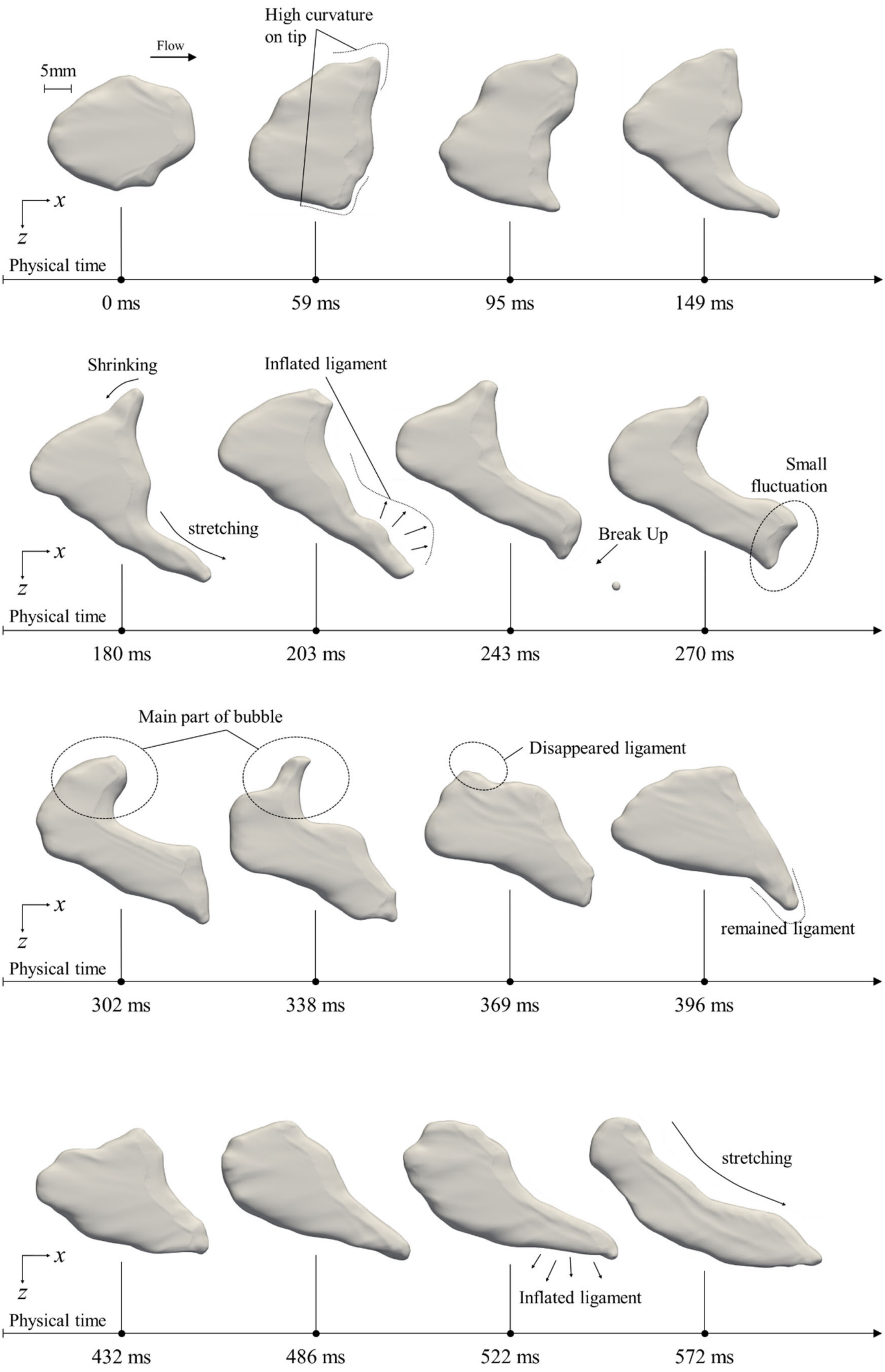

316

317 **Fig. 8** Top view of the bubble shape evolution for case 2

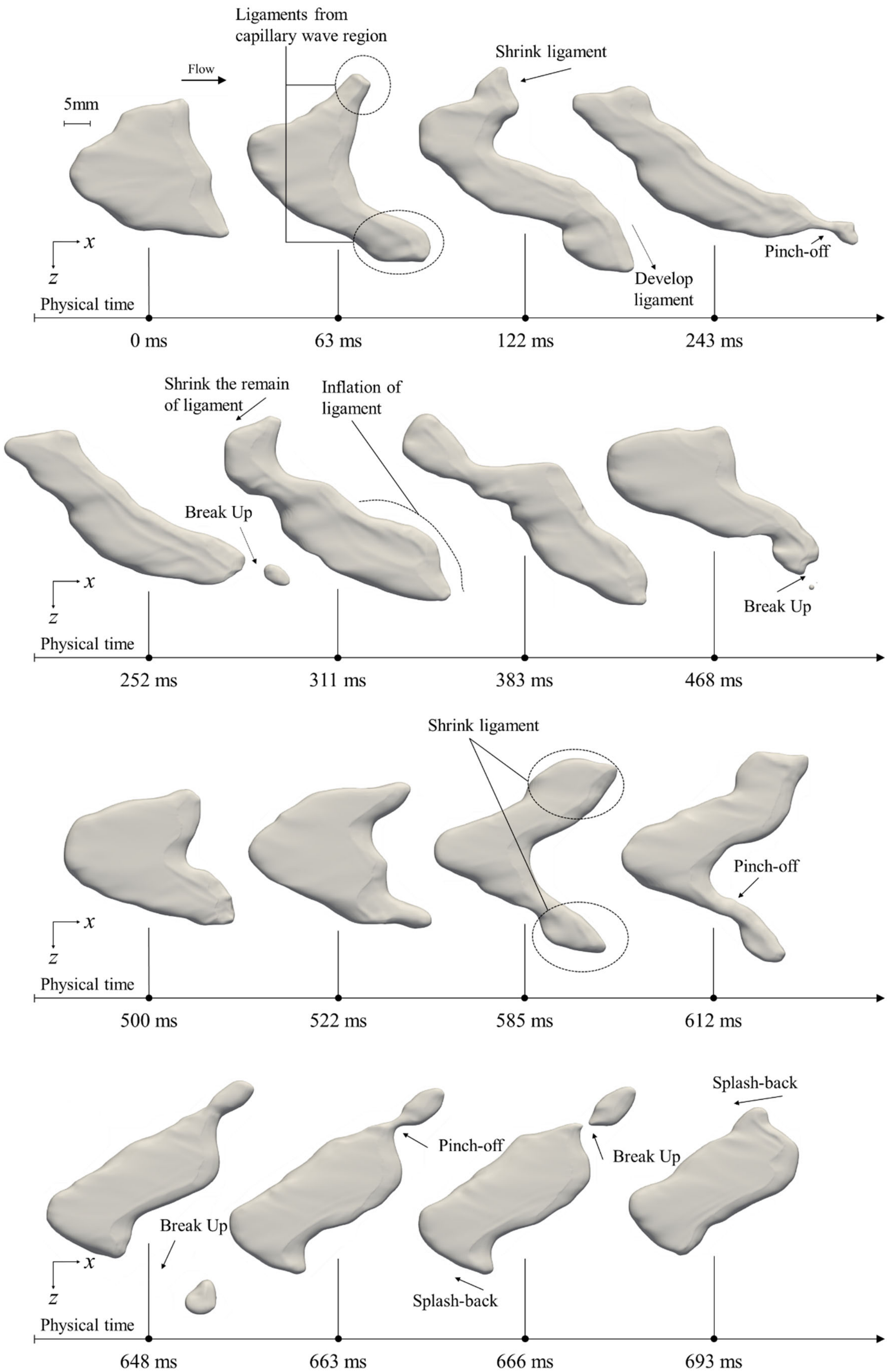

Fig. 9 Top view of the bubble shape evolution for case 3

5.2 Relationship between liquid film thickness and velocity ratio

In this study, we categorized several sequences of the deformation of large-sized bubbles, and the development of ligaments in both directions was confirmed at a Weber number of approximately 300 in turbulent Poiseuille flow, as described by Kim *et al*. (2021). However, in one direction, ligament and inflation were not observed at all, this deformation being considered to be present for large-sized bubbles for the current cases in turbulent Couette flow. Thus, the velocity field around the bubble was investigated based on our knowledge of bubble deformation in Couette flow, as shown in **Fig. 10(a)**.

The bubble in laminar Couette flow deforms linearly; thus, the bubble in turbulent Couette flow exhibits high deformation at its tip owing to the exponential change in velocity near the wall. Consequently, the ligament at the tip may be affected by the velocity around the bubble, while the bottom of the bubble does not reach the bottom of the channel owing to its buoyancy in the wall-normal direction. Therefore, the relationship between the velocity and liquid film thickness was investigated, as shown in **Fig. 10(b)**; the velocity in single-phase flow was obtained at $y^+ = 2.5$.

Figures 11–13 show dimensionless velocity and liquid film thickness for each case. The dimensionless velocity was obtained by dividing the instantaneous velocity by the mean velocity of the single-phase flow at $y^+ = 2.5$, while the dimensionless liquid film thickness was obtained by dividing the liquid film thickness by the half-height of the channel. As shown, the high-velocity region of the ligaments is eventually inflated and stretched for all cases, while the main parts of the bubble gradually shrink. Consequently, the inflating and shrinking of each part of the bubbles is strongly associated with the high flow field in the liquid film. Moreover, the liquid film thickness of these regions are lower than those of other regions.

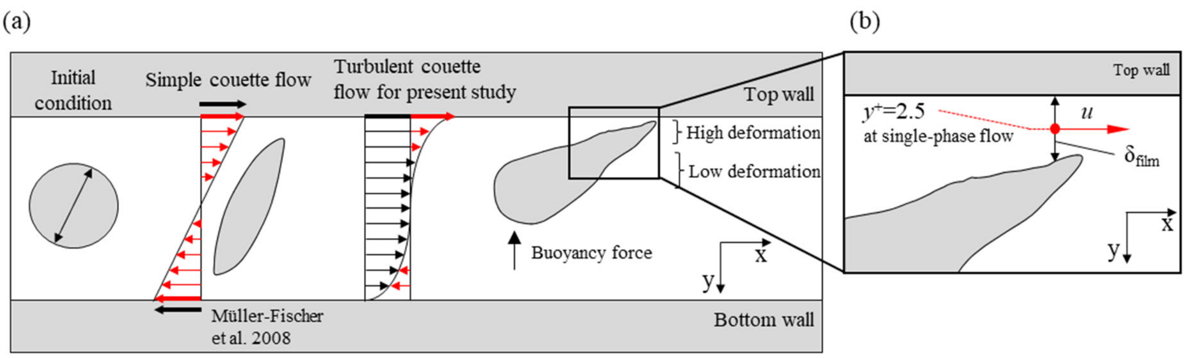

Fig. 10(a) Illustration of bubble deformation at laminar (Müller-Fischer *et al*., 2008) and turbulent Couette flow, (b) Schematic view of liquid film thickness and the height where velocity is obtained.

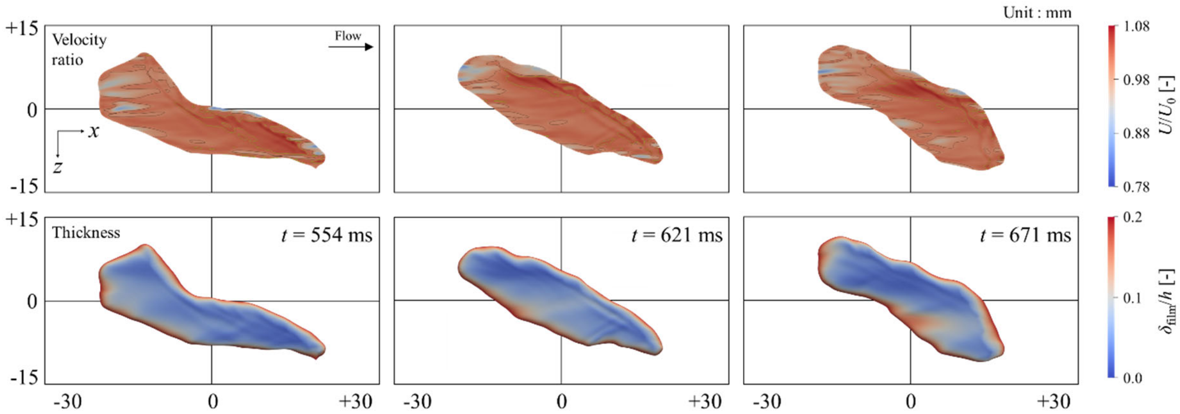

Fig. 11 Dimensionless velocity and liquid film thickness for case 1

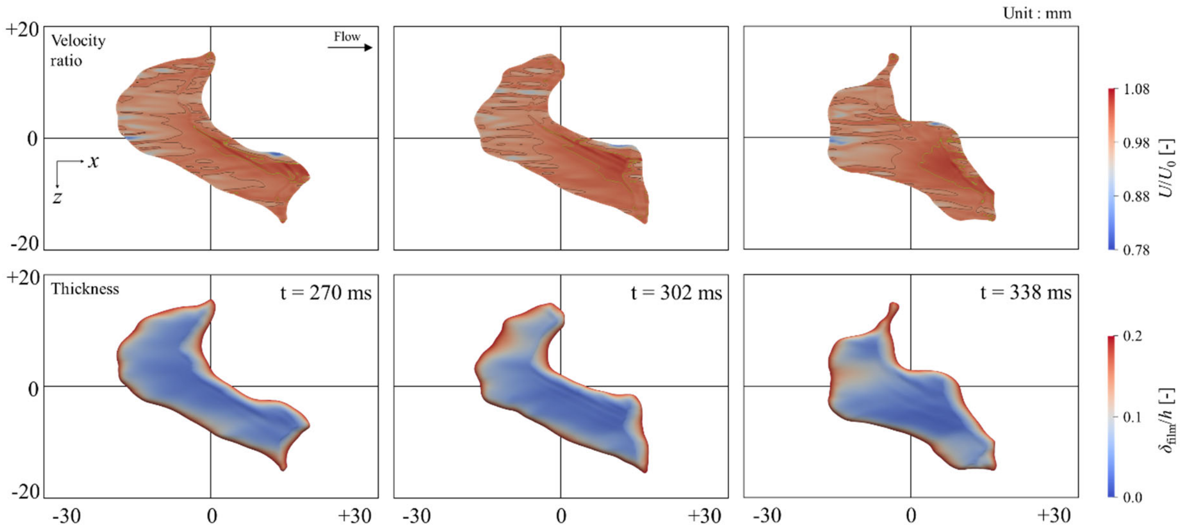

Fig. 12 Dimensionless velocity and liquid film thickness for case 2

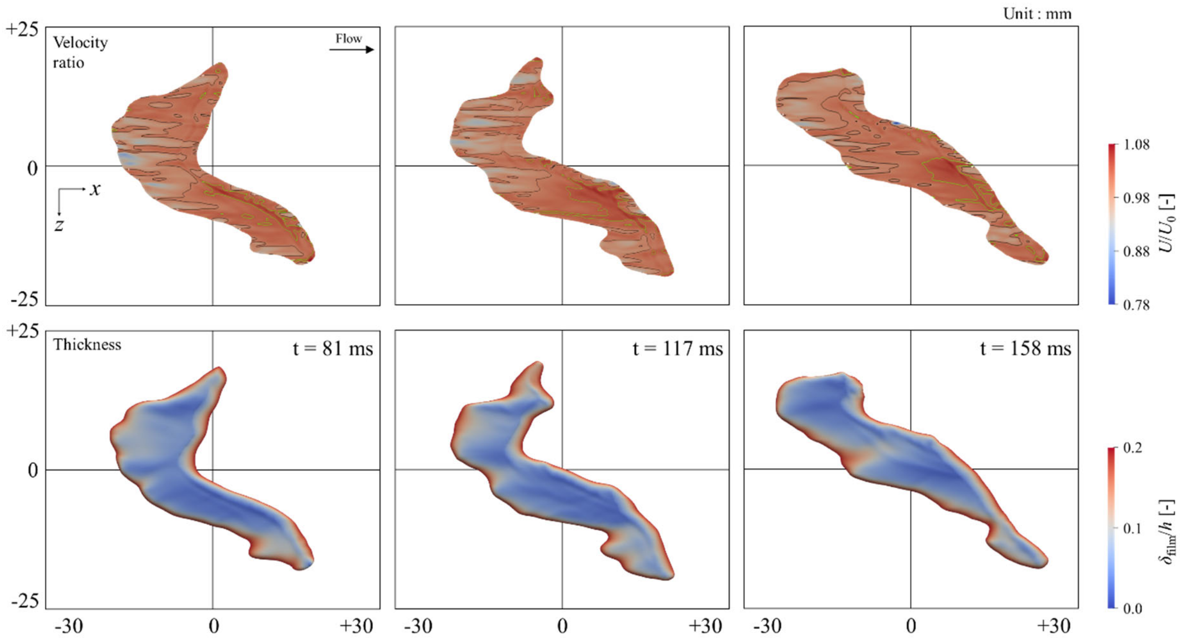

Fig. 13 Dimensionless velocity and liquid film thickness for case 3

Figure 14 shows the relationship between dimensionless velocity and liquid film thickness. The results for each case are compared with the reference case, obtained at a Weber number of 250 in Poiseuille flow. Typically, the dimensionless velocity in Couette flow is distributed widely between 0.8 and 1.05. Meanwhile, there is variation in the time and bubble cases—that is, the data is concentrated, with the dimensionless velocity being inversely proportional to the specific liquid film thickness. The dimensionless velocity increases to approximately 1.05 below $\delta_{film}/h = 0.05$. In the reference case, the distributions are the reverse of those in Couette flow; however, δ_{film}/h is not above 0.05, and exhibits no concentrated trends near $\delta_{film}/h = 0.05$. Thus, the velocity increase in this region and the thinning of the liquid film in Couette flow are considered to cause additional deformation on the tip, similar to the development of the ligament, as shown in **Fig. 15**.

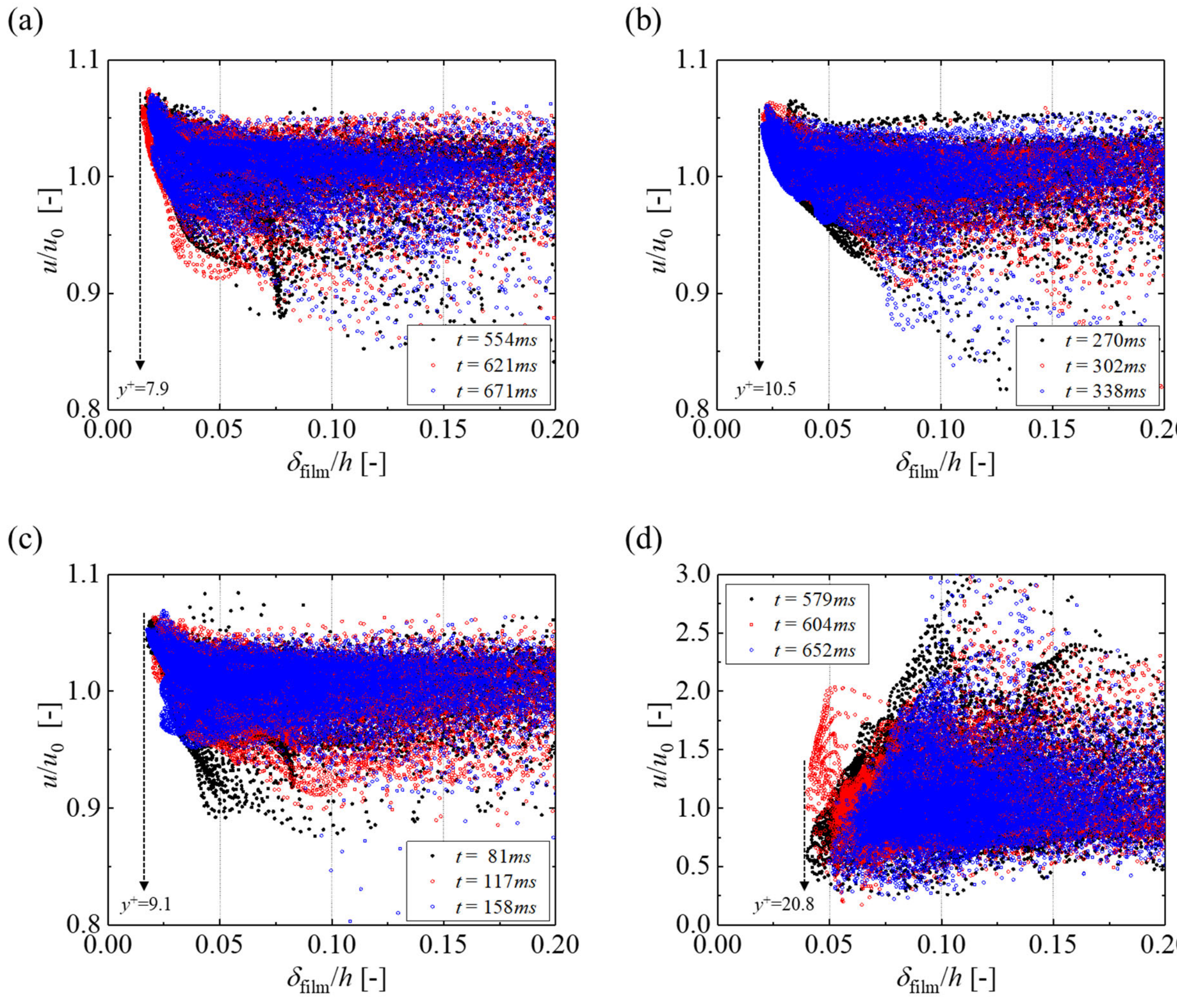

Fig. 14 Scatter plots of the relationship between dimensionless velocity and liquid film thickness. (a) Case 1, (b) Case 2, (c) Case 3, and (d) Reference case, *We* = 250 in Kim *et al*. (2021).

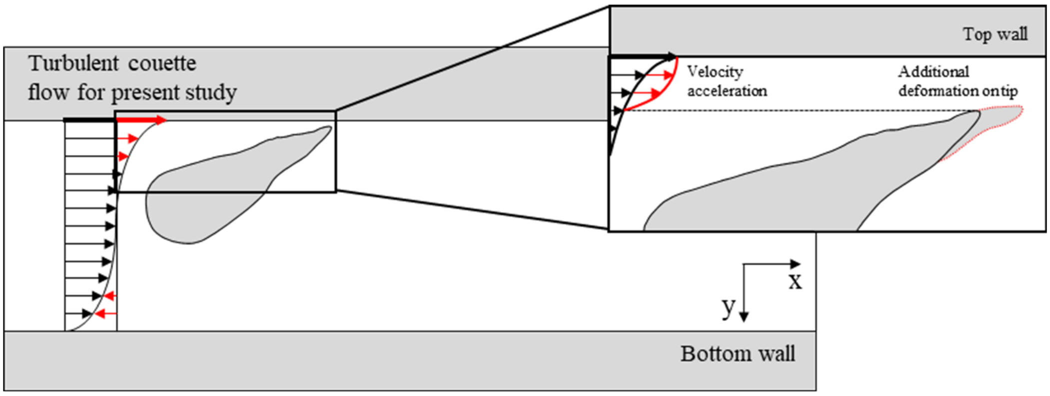

Fig. 15 Velocity acceleration on the liquid film and additional deformation of the tip of the bubble.

6. Conclusions

In this study, a numerical flow visualization of a single large-sized bubble in a turbulent Couette flow was performed. As expected for such a bubble, the representative bubble shape characteristics—such as the liquid film and the capillary wave—were formed in a direction opposite to that in the Poiseuille flow. **Figure 16** shows the physical bubble deformation mechanism in turbulent Couette flow, which is described in detail below.

i) In the initial state, the bubble shows a relatively round shape on the rear side and interface instability on the front side with a high tip curvature in the spanwise direction.

ii) Two types of deformation occur on the front side (ligament)—that is, the first occurs in both directions when the front side is aligned perpendicular to the streamwise direction and the formation of relatively small ligaments is suppressed; the second occurs when the front side is tilted relative to the streamwise direction, this condition occurs frequently and is maintained even when the tip breaks.

iii) A change of the center of gravity (CG) of the bubble could be observed after the one-direction ligament development. This ligament is sometimes larger than the main part of the bubble, causing shrinkage of the main bubble.

iv) Pinch-off and breaking of the ligament occur when it is sufficiently developed. The tip of the ligament frequently breaks and shrinks quickly owing to splash-back. Meanwhile, the large ligament arising from the change in the bubble CG shows only a small fluctuation on the breakup surface and maintains its shape.

v) Deformation to a stable state (similar to the initial stage) occurs after sequences (**iii**) and (**iv**). Interestingly, in most cases, the front side is tilted in a certain direction because of the imbalance in ligament size and change in the bubble CG. Consequently, this condition quickly changes to sequence **(ii)**.

Based on this bubble deformation sequence, we observed the development of ligaments in one direction and the inflation of ligaments with shrinkage of the main part of the bubble. This bubble deformation was dominated by the displacement of the main part of the bubble, which experienced an increase in velocity greater than that during single-phase flow from the liquid film region. From the scatter plot depicting the relationship between the dimensionless velocity and liquid film thickness, it is clear that the increase in velocity occurred below $\delta_{\mathrm{film}}/h = 0.05$.

The bubble cases in this study were limited to a Weber number range of 200–300. Thus, in future work, numerical simulations should be performed for Weber numbers beyond these limits—that is, below 200 and above 300—to generalize the bubble deformation mechanism in turbulent Couette flow.

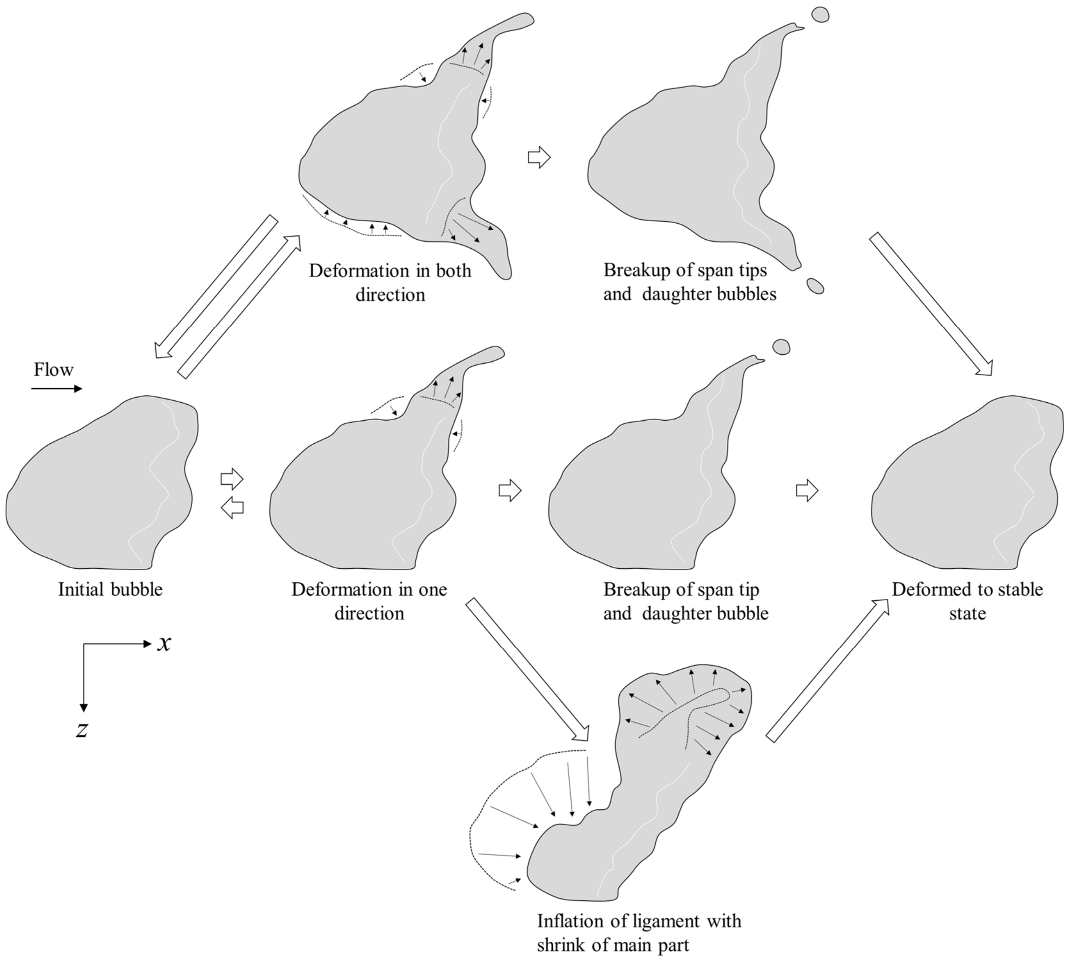

Fig. 16 Schematic of the large-sized bubble deformation sequence in turbulent Couette flow.

Acknowledgments

This work was supported by the MEXT Doctoral program for the Data-Related InnoVation Expert Hokkaido University (D-DRIVE-HU) program; the high-performance computing project (hp200223, hp210160); the Fundamental Research Development Association for Shipbuilding and Offshore (REDAS); and the F3 Engineering Education and Research Center, Faculty of Engineering, Hokkaido University. The authors thank Dr. Yuichi Murai, Hokkaido University, for his valuable discussions on bubble dynamics.

References

Andreolli A, Quadrio M, and Gatti D (2015) Global energy budgets in turbulent Couette and Poiseuille flows. J Fluid Mech 924:A25 https://doi.org/10.1017/jfm.2021.598

Avsarkisov V, Hoyas S, Oberlack M, and García-Galache JP (2014) Turbulent plane Couette flow at moderately high Reynolds number. J Fluid Mech 751:R1 https://doi.org/10.1017/jfm.2014.323

Fokoua NG, Gabillet C, Aubert A, Colin C (2015) Effect of bubble's arrangement on the viscous torque in bubbly Taylor–Couette flow. Phys Fluids 27:034105 https://doi.org/10.1063/1.4915071

Fukuda K, Tokunaga J, Nobunaga T, Nakatani T, Iwasaki T, and Kunitake Y (1999) Frictional drag reduction with air lubricant over super water repellent surface (2nd report): Resistance tests of tanker and high length-to-beam ratio ship models. J Soc NA Jpn 186:73-81. https://doi.org/10.2534/JJASNAOE1968.1999.186_73

Gamet L, Scala M, Roenby J, Scheufler H, Pierson J-L (2020) Validation of volume-of-fluid OpenFOAM® isoAdvector solvers using single bubble benchmarks. Comput Fluids 213: 104722 https://doi.org/10.1016/j.compfluid.2020.104722

Hinze JO (1955) Fundamentals of the hydrodynamic mechanism of splitting in dispersion processes. AIChE J 1:289–295 https://doi.org/10.1002/aic.690010303

Johansen J, Castro AM, and Carrica P (2010) Full-scale two-phase flow measurements on Athena research vessel. Int J Multiphase Flow 36:720–737 https://doi.org/10.1016/j.ijmultiphaseflow.2010.05.002

Kawata T and Tsukahara T (2021) Scale interactions in turbulent plane Couette flows in minimal domains. J Fluid Mech 991:A55 https://doi.org/10.1017/jfm.2020.1063

Katsui T, Okamoto Y, Kasahara Y, Shimoyama N, Iwasaki Y, Soejima S, and Hirayama A (2003) A study of air lubrication method to reduce frictional resistance of ship. *J Kansai Soc NA* Jpn 239:45–53 (in Japanese) https://doi.org/10.14856/jksna.2003.239_45

Kim SW, Oshima N, Murai Y, and Park HJ (2020) Numerical investigation of a single intermediate-sized bubble in horizontal turbulent channel flow. J Fluid Sci Technol 15(3):JFST0020 https://doi.org/10.1299/jfst.2020jfst0020

Kim SW, Oshima N, Murai Y, and Park HJ (2021) Direct numerical simulation of frictional drag modulation in horizontal channel flow subjected to single large-sized bubble injection. Int J Multiphase Flow 145:103838 https://doi.org/10.1016/j.ijmultiphaseflow.2021.103838

Kodama Y, Kakugawa A, Takahashi T, and Kawashima H (2000) Experimental study on microbubbles and their applicability to ships for skin friction reduction. Int J Heat Fluid Flow 21(5):582–588 https://doi.org/10.1016/S0142-727X(00)00048-5

Madavan NK, Deutsch S, and Merkle CL (1984) Reduction of turbulent skin friction by microbubbles. Phys Fluids 27(2):356–363. https://doi.org/10.1063/1.864620

Mäkiharju S A, Elbing BR, Wiggins A, Schinasi S, Vanden-Broeck J-M, Perlin M, Dowling DR, and Ceccio SL (2013) On the scaling of air entrainment from a ventilated partial cavity. J Fluid Mech 732:47–76 https://doi.org/10.1017/jfm.2013.387

McCormick ME and Bhattacharyya R (1973) Drag reduction of a submersible hull by electrolysis. Nav Eng J 85(2):11–16 https://doi.org/10.1111/j.1559-3584.1973.tb04788.x

Merkle CL and Deutsch S (1992) Microbubble drag reduction in liquid turbulent boundary layers. ASME Appl Mech Rev 45(3):103–127 https://doi.org/10.1115/1.3119751

Murai Y, Fujii H, Tasaka Y, and Takeda Y (2006) Turbulent bubbly channel flow investigated by ultrasound velocity profiler. J Fluid Sci Technol 1(1):12-23 https://doi.org/10.1299/jfst.1.12

Murai Y, Fukuda H, Oishi Y, Kodama Y, and Yamamoto F (2007) Skin friction reduction by large air bubbles in a horizontal channel flow. Int J Multiphase Flow 33(2):147–163. https://doi.org/10.1016/j.ijmultiphaseflow.2006.08.008

Murai Y, Oiwa H, and Takeda Y (2008) Frictional drag reduction in bubbly Couette-Taylor flow. Phys Fluids 20(3):034101 https://doi.org/10.1063/1.2884471

Murai Y (2014) Frictional drag reduction by bubble injection. Exp Fluids 55:1773 https://doi.org/10.1007/s00348-014-1773-x

Murai Y, Tasaka Y, Oishi Y, and Takeda Y (2018) Modal switching of bubbly Taylor–Couette flow investigated by particle tracking velocimetry. Exp Fluids 59:164 https://doi.org/10.1007/s00348-018-2620-2

Müller-Fischer N, Tobler P, Dressler M, Fischer P, and Windhab EJ (2008) Single bubble deformation and breakup in simple shear flow. Exp Fluids 45:917–926. https://doi.org/10.1007/s00348-008-0509-1

Oishi Y and Murai Y (2014) Horizontal turbulent channel flow interacted by a single large bubble. Exp Therm Fluid Sci 55:128–139. https://doi.org/10.1016/j.expthermflusci.2014.02.022

Orlandi P, Bernardini M, and Pirozzoli S (2015) Poiseuille and Couette flows in the transitional and fully turbulent regime. J Fluid Mech 770:424–441 https://doi.org/10.1017/jfm.2015.138

Park HJ, Oishi Y, Tasaka Y, Murai Y, and Takeda Y (2009) Turbulent shear control with oscillatory bubble injection. J Phys: Conf Ser 147:012037 https://doi.org/10.1088/1742-6596/147/1/012037

Park HJ, Tasaka Y, Oishi Y, and Murai Y (2015) Drag reduction promoted by repetitive bubble injection in turbulent channel flows. Int J Multiphase Flow 75:12–25 https://doi.org/10.1016/j.ijmultiphaseflow.2015.05.003

Park HJ, Oishi Y, Tasaka Y, and Murai Y (2016) Void waves propagating in the bubbly two-phase turbulent boundary layer beneath a flat-bottom model ship during drag reduction. Exp Fluids 57:178 https://doi.org/10.1007/s00348-016-2268-8

Park HJ, Tasaka Y, and Murai Y (2018) Bubbly drag reduction accompanied by void wave generation inside turbulent boundary layers. Exp Fluids 59:166 https://doi.org/10.1007/s00348-018-2621-1

Park HJ, Tasaka Y, and Murai Y (2019) Bubbly drag reduction investigated by time-resolved ultrasonic pulse echography for liquid films creeping inside a turbulent boundary layer. Exp Therm Fluid Sci 103:66–77 https://doi.org/10.1016/j.expthermflusci.2018.12.025

Park HJ, Tasaka Y, and Murai Y (2022) Spatial development of single void pulse in a horizontal turbulent bubbly channel flow investigated by a time-resolved two-laser measurement. Int J Multiphase Flow 146:103867 https://doi.org/10.1016/j.ijmultiphaseflow.2021.103867

Roenby J, Bredmose H, and Jasak H (2016) A computational method for sharp interface advection. R Soc Open Sci 3:160405 https://doi.org/10.1098/rsos.160405

Sanders WC, Winkel ES, Dowling DR, Perlin M, and Ceccio SL (2006) Bubble friction drag reduction in a high-Reynolds-number flat-plate turbulent boundary layer. J Fluid Mech 552:353–380. https://doi.org/10.1017/S0022112006008688

Tanaka T, Park HJ, Tasaka Y, and Murai Y (2020) Spontaneous and artificial void wave propagation beneath a flat-bottom model ship. Ocean Eng 214:107850 https://doi.org/10.1016/j.oceaneng.2020.107850

Tanaka T, Oishi Y, Park HJ, Tasaka Y, Murai Y, and Kawakita C (2021) Repetitive bubble injection promoting frictional drag reduction in high-speed horizontal turbulent channel flows. Ocean Eng 239:109909 https://doi.org/10.1016/j.oceaneng.2021.109909